This is a non-peer-reviewed preprint submitted to EarthArXiv.

This manuscript has been submitted for publication in Environmental Science & Technology Letters. Please note the manuscript has yet to be formally accepted for publication. Subsequent versions of this manuscript may have slightly different content. If accepted, the final version of this manuscript will be available via the 'Peer-reviewed Publication DOI' link on the right-hand side of this webpage. Please feel free to contact any of the authors; we welcome feedback.

Nanoscale Interfacial Dissolution-Precipitation Reactions Drive Incipient Carbon Mineralization at the Tamarack Intrusive Complex Peridotite

Madeline F. Bartels [a†*], Quin R.S. Miller [a*], Xiaoxu Li [b], C. Heath Stanfield [a], Ruoshi Cao [a], Jose Marcial [a], Emily T. Nienhuis [b], Mathieu Fillion [c], Robert Rush [d], Martin Sauvé [e], H. Todd Schaef [a]

[a] Energy and Environment Directorate, Pacific Northwest National Laboratory, Richland, Washington, USA
[b] Physical and Computational Sciences Directorate, Pacific Northwest National Laboratory, Richland, Washington, USA
[c] Rio Tinto, Montréal, Québec, Canada
[d] Rio Tinto, Salt Lake City, Utah, USA
[e] Rio Tinto, Ulaanbaatar Hot, Mongolia
[†] Current affiliation is Department of Earth, Energy, & Environment, University of Calgary, Calgary, AB, Canada

KEYWORDS: carbon mineralization, critical mineral recovery, IL-TEM, nickel, peridotite

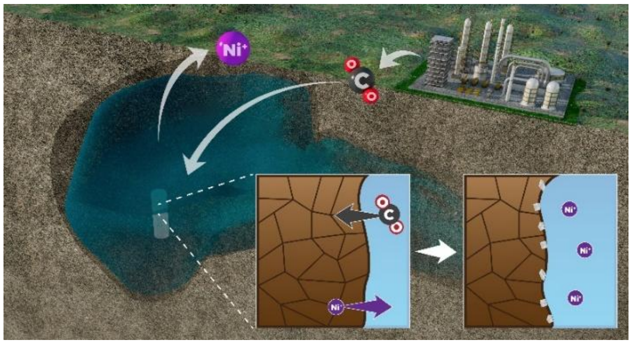

ABSTRACT: The Tamarack ultramafic intrusion in Minnesota, USA may be suited to host concurrent carbon sequestration and critical mineral recovery. These dual capabilities are vital to reduce carbon emissions and supply metals (e.g. nickel) necessary for electric vehicles and other rapidly upscaling energy technologies. To understand carbonation reaction pathways and assess carbon sequestration potential in the Tamarack Intrusive Complex (TIC), we reacted a suite of Tamarack Bowl intrusion olivine (BIO) samples with aqueous-dissolved and liquid or supercritical CO_2 ($scCO_2$) at 90 bar and 21-90 °C to simulate a range of subsurface conditions. Samples were characterized pre- and post-reaction with multiple geochemical and mineralogical techniques, and results indicate mineral dissolution followed by magnesite precipitation. Pseudo in situ Identical Location Transmission Electron Microscopy (IL-TEM) experiments revealed that a carbonation reaction of TIC BIO peridotite with water-saturated $scCO_2$ formed aragonite nanocrystals on an altered plagioclase surface and induced dissolution of nickel-bearing forsteritic olivine. The presence of nanoscale-resolved carbonation products identified by IL-TEM, coupled with carbonate transformation rates quantified in batch reactions, suggests that the TIC BIO resource can conservatively store 320-1,070 million metric tonnes (MMT) of CO_2 via mineralization while mobilizing 0.9-3.1 MMT of nickel if only 5% of the TIC rock volume is accessed.

SYNOPSIS: Carbon-negative critical mineral mining can be implemented in the Tamarack Intrusive Complex peridotite, USA via deep in situ leaching with CO_2-H_2O fluids.

INTRODUCTION

Carbon capture and storage (CCS) technologies are upscaling as part of a growing portfolio of energy security approaches. Carbon mineralization is an optimal carbon storage method because it is durable, permanent on geologic timescales[1, 2], and thermodynamically favorable[3]. A growing body of work has identified carbon mineralization pathways and discussed opportunities and challenges for in situ[4-6], ex situ[7-9], and enhanced weathering[10, 11] carbon sequestration. Pilot studies in the USA[12, 13], Iceland[14, 15], Oman[16, 17], and Saudi Arabia[18] have demonstrated that the injection of CO_2 into mafic-ultramafic reservoirs has the potential to permanently store vast amounts of carbon in the form of stable carbonate minerals.

Additionally, in situ carbon sequestration has the potential to supply value added products as an unconventional source of critical minerals[19, 20]. Critical materials such as nickel, cobalt, and rare earth elements are used to produce renewable energy technologies including durable batteries used in Artificial Intelligence data centers and electric vehicles[21]. The exploration and production of these materials must rapidly increase to meet the growing global need for widely deployable energy and computing technologies. As nickel demand alone is expected to triple by 2030[22], new mining and chemical recovery strategies must come into play to ensure a robust and sustainable use of diminishing natural resources. Recent work has investigated geochemical pathways to couple the dual climate goals of durable carbon storage and enhanced mineral recovery[20, 23-26], an aim that would facilitate a carbon-negative critical mineral supply chain[27].

The Tamarack project is an undeveloped high-grade nickel deposit in Minnesota, United States.[28] This site is of potential interest for demonstrating the integration of durable carbon storage with the Ni mining process, including in olivine-rich peridotite resources that lack what are traditionally considered to be high-grade economical sulfide-rich ores. Carbon captured from regional point sources could conceivably be transported to the Tamarack project and injected as liquid (l), supercritical (sc), and/or aqueous (aq) CO_2 into the subsurface, leading to the dissolution of mafic-ultramafic host rock and the formation of stable carbonate minerals[29, 30]. Injected CO_2 will also act to leach nickel from olivine in host rock, potentially allowing for enhanced critical mineral recovery from the aqueous fluid phase[31]. Herein, we investigate carbon mineralization reactions of Tamarack rocks as part of an effort to assess the potential for critical mineral recovery with carbon storage in ultramafic resources. We first investigated carbonation pathways in batch reaction experiments at a range of subsurface conditions before turning to state-of-the-art transmission electron microscopy reaction monitoring techniques[32] to probe spatially resolved, nanoscale changes at the mineral-fluid interface.

METHODS AND MATERIALS

Geologic Background and Sample Preparation. The Tamarack Intrusive Complex (TIC) is part of the larger Midcontinent Rift system stretching across much of the midwestern United States. The TIC is comprised of two primary mafic-ultramafic magmatic intrusions: the "dike" intrusion to the north and the "bowl" intrusion to the south. The dike region hosts disseminated Ni-rich sulfide mineralization and records a history of multiple magmatic pulses that formed a coarse-grained olivine (CGO) unit and a fine-grained olivine (FGO) unit. The Tamarack Bowl is a potentially porous and permeable peridotite unit composed largely of fine-grained olivine (**Figure S1**). It is overlain by a gabbro-gabbronorite caprock[33-35]. In this work, we refer to the olivine retrieved from the Tamarack Bowl and discussed in this work as Bowl intrusion olivine (BIO) to distinguish it from FGO hosted in the TIC dike.

Two sample sets were collected from the BIO region of the Tamarack Intrusive Complex (TIC) shown in **Figure S1**. The Tamarack Bowl-1 sample was retrieved from 588 m depth in the 10TK0128 Tamarack borehole, and the Tamarack Hybrid sample was created from a mixture of three core samples collected from two historic boreholes (177-215 m depth) in the TIC's BIO region. These cores were dry sieved into a 0.425- 2 mm size fraction and portions of the Bowl-1 and Hybrid samples were ground in an agate mortar and pestle to a fine powder for analysis.

Sample Characterization Techniques. The characterization of unreacted Tamarack samples was accomplished with a suite of analytical techniques. First, Bowl-1 and Hybrid samples were analyzed with powder X-ray diffraction (XRD) to resolve original mineral phases, which were identified using the Eva software and quantified using the TOPAS software (**Table S1**). The samples' carbonate mineral content was quantified with thermogravimetric analysis-mass spectrometry (TGA-MS). Helium pycnometry (**Table S2**) yielded a rock density of 3.31 g/cm^3 (an average of the Bowl-1 and Hybrid sample densities of 3.27 g/cm^3 and 3.35 g/cm^3, respectively). Electron probe microanalysis (EPMA) on the Bowl-1 sample yielded a spatially resolved geochemical composition for the grain surface (**Table S3**) and was particularly helpful in identifying and visualizing critical metal distribution. These methods are further described in the **Supporting Information.**

Batch Reactor Experiments and Carbonation Rate Quantification. After thorough characterization, the Bowl-1 and Hybrid samples were reacted in a static Parr vessel batch experiment with aqueous-dissolved CO_2 and wet $scCO_2$. For ease of notation, we designate $scCO_2$ to refer to non-aqueous CO_2 injected as a liquid for the 21 °C batch experiment and a supercritical fluid for the 50 and 90 °C experiments. Experimental conditions were chosen to simulate reservoir conditions and procedures are described further in the **Supporting Information**. Samples recovered at multiple reaction timesteps were mineralogically and compositionally characterized by XRD and TGA-MS. Carbonate mineral mass was determined by measuring samples' evolved CO_2 ion current with TGA-MS and comparing against a calcium oxalate monohydrate calibration curve, as recently described[36]. Carbonation efficiency was obtained by plotting Tamarack samples' evolved CO_2 ion current area against calibration curves[37]. Measurements were conducted in triplicate and yielded a standard deviation of 0.025 wt%.

Identical Location Transmission Electron Microscopy (IL-TEM). We used our recently-developed IL-TEM methodology[32] for evaluating carbonation reactions to understand dissolution-precipitation reactions happening at the grain-fluid interface. Nanoscale-resolved crystallographic images of identical grain locations before and after reaction of a Bowl-1 sample with $scCO_2$ in a Parr vessel at 50 °C and 90 bar were obtained with TEM and Energy-Dispersive Spectroscopy. IL-TEM methods are further described in Li et al.[32] and in the **Supporting Information**.

RESULTS AND DISCUSSION

Chemical Composition and Mineralogy of Unreacted Tamarack Samples. The geochemical and mineralogical analyses described in the methods revealed the unreacted Tamarack samples to be composed predominantly of un-serpentinized peridotite. XRD-probed mineral assemblages consist primarily of a forsteritic olivine phase (65 wt%) with significant pyroxene and calcic plagioclase feldspar (anorthite) and minor chlorite, hornblende, magnesite, and talc. These results are generally consistent with previously reported compositions for the TIC[33, 35]. EPMA analysis on the Bowl-1 olivine grains revealed a composition of Fo_{77} to Fo_{83} ($Mg_{1.54}Fe_{0.46}SiO_4$ to $Mg_{1.66}Fe_{0.34}SiO_4$), with 1651-2044 ppm Ni in the olivine. This forsteritic composition was consistent with our XRD results interpreted using structure-composition relationships for olivine[38], which resulted in an estimated composition of Fo_{82} ($Mg_{1.64}Fe_{0.36}SiO_4$). Spatially resolved geochemical and mineralogical data from XRD and EPMA are shown in **Figures S2**-**S4**.

TGA-MS data for the unreacted Tamarack Bowl-1 and Hybrid samples show a 2.2% and 1.9% respective mass loss during heating coincident with a bimodal release of CO_2 over a temperature range consistent with the presence of magnesite ($MgCO_3$)[39-41]. Calculations indicate a 2.50 wt% and 2.45 wt% magnesite abundance for the Bowl-1 and Hybrid samples, respectively. No evidence for the presence of calcite, which decomposes at higher temperatures than magnesite (~900 °C[42] compared to ~600-650 °C[43]), was observed in TGA-MS analysis.

Magnesite Dissolution and Precipitation in Batch Reactor Experiments. Following 38- and 90- day batch reaction experiments, the Hybrid BIO samples were recovered and characterized to detect and quantify changes due to olivine dissolution, carbonate formation, and secondary mineral alteration. Subtle carbonate mineral changes observed via TGA-MS were the most salient indicator of carbon mineralization in our experiments. Weight loss due to preexisting carbonate decomposition and evolved CO_2 ion current peaks obtained from TGA-MS for Hybrid BIO samples reacted with $scCO_2$ at 50-90 °C and 90 bar are plotted in **Figure 1.** The results for the 38-day reacted samples indicate that magnesite dissolution occurred. In $scCO_2$ experiments, magnesite reprecipitated and/or precipitated after 90 days. In CO_2 (aq) experiments, magnesite continued to experience net dissolution during the 90 days of reaction.

An examination of evolved CO_2 ion current curves reveals changes in carbonate mineral assemblages during early-stage carbonation. For Hybrid BIO samples reacted with CO_2 (aq) for 90 days, a low temperature (~350-500 °C) evolved CO_2 ion current peak was observed in the TGA-MS data (see **Figure 1c-d**) in addition to the large peak at ~600 °C consistent with magnesite's thermal decomposition range[43]. This broad CO_2 ion current peak at ~400 °C potentially indicates the formation of an amorphous carbonate during the early precipitation phase, following from previous studies[44, 45]. In unreacted Hybrid samples, a minor shoulder at the ~650 °C peak suggests the presence of a Ca-bearing carbonate which is reordered and/or dissolved by 38 days of reaction with $scCO_2$ or CO_2 (aq), based on the disappearance of

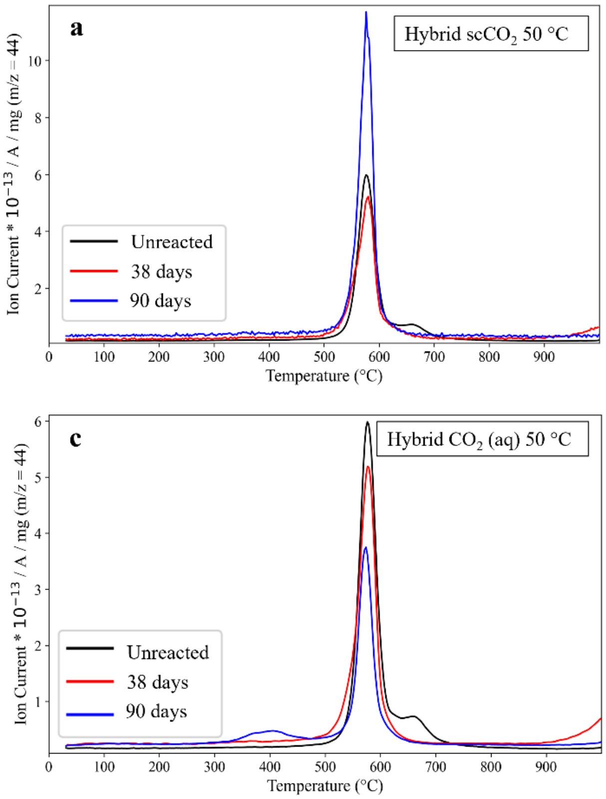

Figure 1. Evolved CO_2 ion current curves for Parr vessel carbonation experiments of a Tamarack Hybrid sample (0.425- 2mm size fraction) reacted with supercritical CO_2 ($scCO_2$) and aqueous CO_2 (CO_2 (aq)) at 90 bar, 50 °C and 90 °C. Experiment details are found in **Table S4**. Sample mass loss in the 550-650 °C temperature range is due to magnesite decomposition to MgO and CO_2. The coupled mass spectrometer measures CO_2 (m/z 44) ion current and the amount of CO_2 released is quantified by taking the area under the curve. (a, b) Plots of $scCO_2$ carbonation reactions indicate magnesite dissolution (38 days) followed by precipitation/reprecipitation (90 days), with total net precipitation. (c, d) Plots of CO_2 (aq) carbonation reactions indicate net magnesite dissolution up to 90 days reaction time.

this shoulder in the reacted sample. The rapid dissolution rate of Ca-rich carbonates compared to Mg-rich carbonates[46] further indicates that this phase is Ca-bearing. Because its decarbonation temperature is lower than that of a fully crystalline calcium carbonate[42], we assume this phase is a unique Ca-Mg carbonate and/or a small sized, poorly crystalline Ca-carbonate, noting that smaller crystal size also decreases decarbonation temperature in carbonates[42].

Figure 2 illustrates the changes in magnesite abundance as a function of reaction time and differentiates between Bowl-1 and Hybrid samples, $scCO_2$ and CO_2 (aq) reaction fluids, and 50 °C and 90 °C experiments. Bowl-1 sample grains were smaller in diameter than Hybrid sample grains and thus provided larger surface areas to host carbonation reactions. Because larger surface areas enable faster reaction times, the 56 day, 90 °C Bowl-1 batch reacted sample did not capture initial magnesite dissolution and post-reaction characterization identified only an increase in magnesite abundance from reprecipitation and precipitation. Similar trends were observed in the 160 day, 50 °C reaction of the Bowl-1 sample with $scCO_2$.

Despite the trend of magnesite dissolution and precipitation in Hybrid $scCO_2$-reacted samples as indicated by TGA-MS weight loss (shown in **Figure S5**) and evolved CO_2 ion current curves (**Figure 1**), CO_2 (aq)-reacted samples exhibit continuous magnesite dissolution up to 90 days of reaction. These distinct trends can be explained when considering the fluid component of batch reaction experiments. The carbonation of rock with wet $scCO_2$ occurs within a thin water film formed at the mineral- fluid interface[47]. This thin water film hosts dissolved CO_2 and functions as a reaction site that is continually replenished when kept at constant Parr vessel head pressure. At the same time, Ca, Mg, Fe, Ni, and other cation concentrations in these water films increase with reaction time. Assuming a thin water film thickness of 1 nm[47], we calculate the water:rock mass ratio of $scCO_2$ experiments to be 0.0017 when using only the mass of water capable of grain contact, i.e. thin water films. In our batch reaction CO_2 (aq) carbonation experiments, the water:rock mass ratio is 6 and dissolved metal cations access the entire water volume. With a nearly 3500 times smaller water:rock mass ratio for wet $scCO_2$ compared to CO_2 (aq) experiments, metal cations released from dissolving olivine reach saturation much faster in $scCO_2$ thin water films than CO_2 (aq) bulk water. As olivine dissolution persists, cations (e.g. Mg^{2+}) react with bicarbonate to precipitate carbonate minerals. These distinct saturation paradigms with regard to carbonate saturation conditions likely explain why magnesite precipitation and/or reprecipitation is observed in $scCO_2$ but not CO_2 (aq) experiments.

Though magnesite did not reprecipitate after 90 days of reaction with CO_2 (aq), batch reaction results suggest that Tamarack sample grains can successfully dissolve in a CO_2-rich system. Because olivine dissolves more readily than carbonate at reservoir conditions[48], magnesite dissolution detected by TGA-MS indicates that Tamarack olivine has dissolved to an equal or greater extent. Olivine dissolution provides the cations required to mineralize CO_2 as carbonate minerals and is most often the rate-limiting step in successful in situ carbon mineralization experiments and projects[49, 50]. Although the observed magnesite dissolution and reprecipitation suggests successful mafic and ultramafic mineral-hosted cation mobilization, we turn to IL-TEM to understand carbonation reaction pathways at the mineral surface.

Nanoscale Carbonation Pathways for Olivine and Plagioclase Feldspar Revealed with IL-TEM. The TEM images in **Figure 3** were produced by probing two identical locations on the Bowl-1 surface before and after a 21-day reaction with $scCO_2$ at 50 °C and 90 bar. Images show clear alteration of the entire imaged mineral surface and reveal nanoscale, location-specific carbonate mineral formation.

An amorphous layer with a disordered and lowly crystalline structure formed on a Bowl-1 anorthite grain during batch reaction with $scCO_2$ (**Figure 3a-e**). The presence of this ~4 nm thick layer aligns with recent literature observations of nanoscale passivation layers formed on carbon mineralization materials at mineral-fluid interfaces[47] and could suggest successful mobilization of critical elements into the fluid phase. An aragonite crystal of ~5 nm diameter precipitated on top of the amorphous layer, emphasizing the carbon mineralization potential of non-olivine mineral constituents.

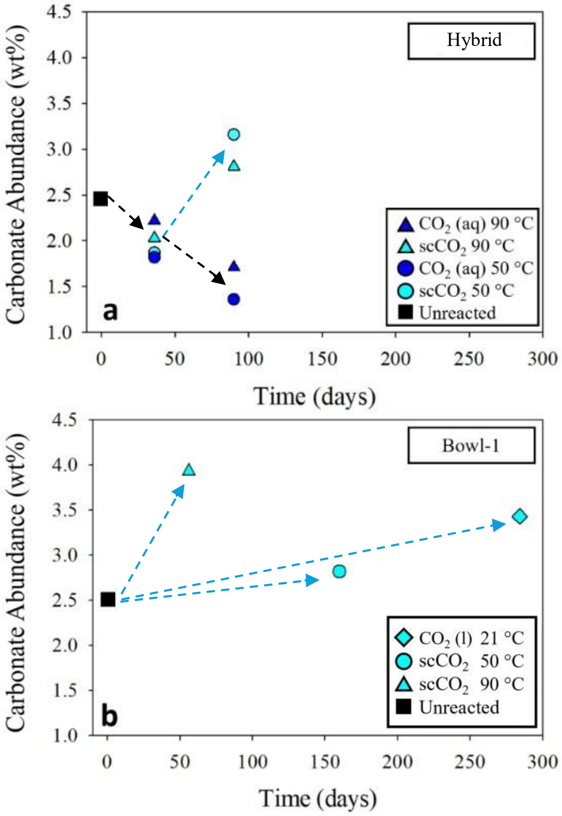

Figure 2. (a) Magnesite weight percent calculations obtained from TGA-MS measurements indicate magnesite dissolution followed by precipitation in Hybrid samples reacted with $scCO_2$ and continuous magnesite dissolution in Hybrid samples reacted with CO_2 (aq). (b) Net magnesite precipitation occurs in both Bowl-1 experiments. Dashed arrows highlight inferred reaction paths.

At another imaging location, exposure to CO_2 produced an altered layer of ~10 nm depth on a previously ordered forsterite grain (**Figure 3f-g**). Recession of the forsterite edge from the lower left image boundary indicates olivine dissolution and suggests a release of cations to the reaction fluid. Again, these results point to the likely mobilization of critical elements such as nickel from the olivine structure upon interaction with $scCO_2$. We calculated a 0.02 nm/hr olivine dissolution rate and a 0.008 nm/hr plagioclase feldspar dissolution rate by coupling reaction time to the spatial extent of mineral alteration resolved by IL-TEM. The overall differences between the olivine and anorthite reaction rates are consistent with the disparity between their respective dissolution rates.[48]

Outlooks on Incipient Carbon Mineralization Reaction Pathways. Mafic-ultramafic mineral alteration and dissolution provides a key pathway for critical element mobilization. IL-TEM images of anorthite dissolution and forsterite alteration indicate the potential of these minerals to release energy-relevant critical mineral elements such as nickel during exposure to CO_2. In addition, carbonate crystal formation on olivine grain surfaces is observed with

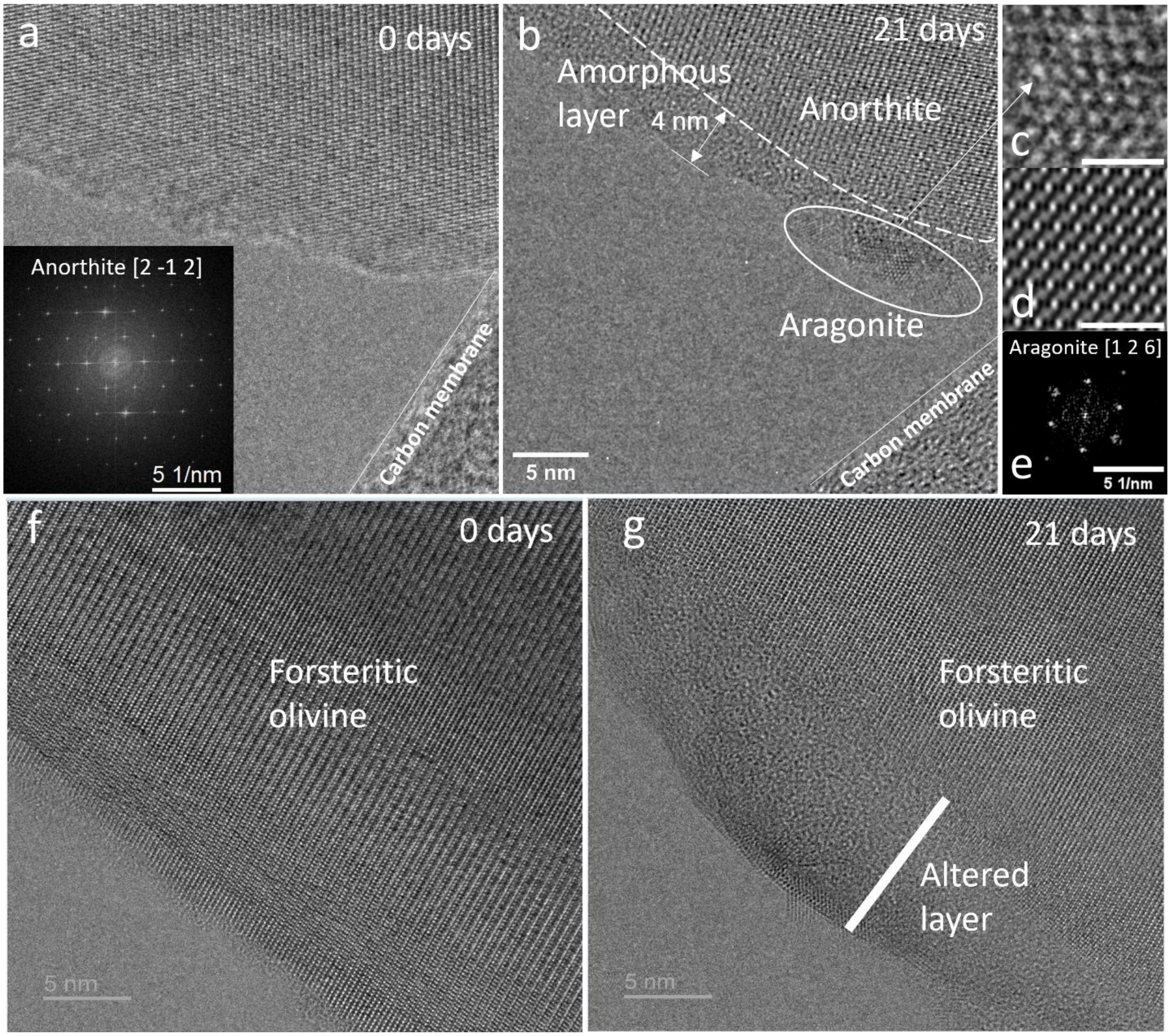

Figure 3. IL-TEM images for unreacted and reacted Tamarack BIO samples. Batch reaction with $scCO_2$ ran for 21 days at 50 °C and 90 bar. (a) Unreacted anorthite in a Bowl-1 grain, with an insert of anorthite's [2 -1 2] plane crystal structure. (b) TEM image of the identical grain location post-reaction shows a ~4 nm thick amorphous layer and nano-aragonite crystals forming on anorthite. (c, d) Closer image of aragonite atoms and structure and (e) aragonite crystal structure on the [1 2 6] plane. (f) Forsteritic olivine in an unreacted Bowl-1 grain with (g) a ~10 nm thick surface alteration layer observed post-reaction.

nanoscale IL-TEM and demonstrated by batch reaction experiments of Tamarack peridotite.

We calculate a conservative CO_2 storage capacity of the TIC BIO's olivine component, assuming that an injected fluid accesses only 5% of the reservoir's reactive surface area and all liberated Mg and Fe cations bind with CO_2 to form Mg-Fe carbonate minerals. We determined a mineralization-based carbon storage potential range by varying potential accessible TIC BIO reservoir volumes from 18 km^3 [28, 33, 51, 52] to 12 and 6 km^3. In a similar way, we incorporate estimated formation porosities of 5%, 10%, and 15%. A rock density of 3.31 g/cm^3, an olivine abundance of 65 wt%, and an olivine composition of Fo_{83} ($Mg_{1.66}Fe_{0.34}SiO_4$) were used in all calculations. These resource estimate calculations for CO_2 mineralization and Ni recovery indicate that the olivine component of the Tamarack Bowl intrusion can conservatively store 320-1,070 million metric tonnes (MMT) of CO_2 (**Table S5**). For context, this far surpasses the goal of the US Department of Energy's CarbonSAFE program to geologically store 50 MMT of CO_2 over 30 years[53]. Dissolution of merely 5% of the reservoir's olivine could mobilize 0.9-3.1 MMT of Ni (**Table S5**), assuming an average of 1700 ppm Ni in the Tamarack BIO unit. Nickel recovery from only 5% of an 18 km^3 TIC BIO resource could supply 30-60 times the USA's annual 8,000-17,000 tonne nickel production[54]. Additionally, successful recovery and processing of this nickel from what is traditionally not considered a target asset could sustain the USA's nickel supply for 50-100 years, even when applying a 300% production rate increase to meet the tripling in demand expected by 2030[22].

When applying our geochemical characterization to estimate the theoretical outcomes of mineral-fluid interactions, the Tamarack site has potential to permanently sequester hundreds of millions of tonnes of CO_2 via mineralization while mobilizing Ni for recovery. Geochemical and mineralogical characterization highlights the overall potential of the TIC BIO and batch reactions reveal coupled and overlapping dissolution-precipitation processes. Evidence of carbonate mineral formation concurrent with olivine dissolution identified by nanoscale resolved IL-TEM suggests that the BIO may be an ideal site to support the development of integrated carbon storage and enhanced mineral recovery. When scaled to a commercial level at the Tamarack and beyond, this process may enable the mining industry to support domestic energy security through the development of multiple current, emerging, and novel energy technologies (e.g., electric vehicles, batteries) for decades to come.

ASSOCIATED CONTENT

Supporting Information. This material is available free of charge on the ACS Publications website at **http://pubs.acs.org**.

> Methods for helium pycnometry, EPMA, TGA-MS, XRD, batch reaction carbonation experiments in Parr vessels, and IL-TEM. Figures of sample locations (Figure S1), select XRD and EPMA data of unreacted sample (Figure S2), EPMA on two unreacted sample grains (Figure S3 and S4), and TGA-MS evolved CO_2 ion current peaks for all batch reaction samples (Figure S5). Tables of quantitative XRD-derived mineralogy (Table S1), helium pycnometry-derived sample densities (Table S2), EPMA oxide abundances of the Bowl-1 sample (Table S3), batch reaction experimental conditions (Table S4), and carbon mineralization potential and Ni mobilization estimates (Table S5).

AUTHOR INFORMATION

Corresponding Authors

*Corresponding Authors

Madeline F. Bartels
madeline.bartels@ucalgary.ca
Quin R.S. Miller
quin.miller@pnnl.gov

Notes

The authors declare no competing financial interests.

ACKNOWLEDGEMENTS

This work was supported by Dr. Douglas Wicks and Dr. Emily Kinser through the Advanced Research Projects Agency-Energy (ARPA-E) Open 2021 Control # 2459-4105, Assessment of the CO_2 Mineralization Potential of Tamarack's Ultramafic Bowl-Shaped Intrusion. MFB was partially supported by the U.S. Department of Energy, Office of Science, Office of Workforce Development for Teachers and Scientists (WDTS) under the Science Undergraduate Laboratory Internships Program (SULI). The information, data, or work presented herein was funded in part by the ARPA-E, U.S. Department of Energy. The views and opinions of authors expressed herein do not necessarily state or reflect those of the United States Government or any agency thereof.

REFERENCES

1.Renforth, P.; Henderson, G., Assessing ocean alkalinity for carbon sequestration. Reviews of Geophysics 2017, 55 (3), 636-674.

2.Hartmann, J.; West, A. J.; Renforth, P.; Köhler, P.; De La Rocha, C. L.; Wolf-Gladrow, D. A.; Dürr, H. H.; Scheffran, J., Enhanced chemical weathering as a geoengineering strategy to reduce atmospheric carbon dioxide, supply nutrients, and mitigate ocean acidification. Reviews of Geophysics 2013, 51 (2), 113-149.

3.Gadikota, G., Carbon mineralization pathways for carbon capture, storage and utilization. Commun Chem 2021, 4 (1), 23.

4.Cao, X.; Li, Q.; Xu, L.; Tan, Y., A review of in situ carbon mineralization in basalt. Journal of Rock Mechanics and Geotechnical Engineering 2024, 16 (4), 1467-1485.

5.Kelemen, P.; Benson, S. M.; Pilorgé, H.; Psarras, P.; Wilcox, J., An Overview of the Status and Challenges of CO2 Storage in Minerals and Geological Formations. 2019, 1 (9).

6.Snæbjörnsdóttir, S. Ó.; Sigfússon, B.; Marieni, C.; Goldberg, D.; Gislason, S. R.; Oelkers, E. H., Carbon dioxide storage through mineral carbonation. Nat. Rev. Earth Environ. 2020, 1 (2), 90-102.

7.Liu, H.; Lu, H.; Hu, H., CO2 capture and mineral storage: State of the art and future challenges. Renewable and Sustainable Energy Reviews 2024, 189, 113908.

8.Kelemen, P. B.; McQueen, N.; Wilcox, J.; Renforth, P.; Dipple, G.; Vankeuren, A. P., Engineered carbon mineralization in ultramafic rocks for CO2 removal from air: Review and new insights. Chemical Geology 2020, 550, 119628.

9.Kirmani, F. U. D.; Raza, A.; Ahmad, S.; Arif, M.; Mahmoud, M., A holistic overview of the in-situ and ex-situ carbon mineralization: Methods, mechanisms, and technical challenges. Science of The Total Environment 2024, 943, 173836.

10.te Pas, E. E. M.; Hagens, M.; Comans, R. N. J., Assessment of the enhanced weathering potential of different silicate minerals to improve soil quality and sequester CO2. Frontiers in Climate 2023, 4.

11.Renforth, P., The negative emission potential of alkaline materials. Nature communications 2019, 10 (1), 1401.

12.McGrail, B. P.; Schaef, H. T.; Spane, F. A.; Cliff, J. B.; Qafoku, O.; Horner, J. A.; Thompson, C. J.; Owen, A. T.; Sullivan, C. E., Field validation of supercritical CO2 reactivity with basalts. Environ. Sci. & Technol. Lett. 2017, 4 (1), 6-10.

13.White, S. K.; Spane, F. A.; Schaef, H. T.; Miller, Q. R.; White, M. D.; Horner, J. A.; McGrail, B. P., Quantification of CO2 mineralization at the Wallula basalt pilot project. Environmental Science & Technology 2020, 54 (22), 14609-14616.

14.Matter, J. M.; Stute, M.; Snæbjörnsdottir, S. Ó.; Oelkers, E. H.; Gislason, S. R.; Aradottir, E. S.; Sigfusson, B.; Gunnarsson, I.; Sigurdardottir, H.; Gunnlaugsson, E.; Axelsson, G.; Alfredsson, H. A.; Wolff-Boenisch, D.; Mesfin, K.; Taya, D. F. d. l. R.; Hall, J.; Dideriksen, K.; Broecker, W. S., Rapid carbon mineralization for permanent disposal of anthropogenic carbon dioxide emissions. Science 2016, 352 (6291), 1312-1314.

15.Pogge von Strandmann, P. A. E.; Burton, K. W.; Snæbjörnsdóttir, S. O.; Sigfússon, B.; Aradóttir, E. S.; Gunnarsson, I.; Alfredsson, H. A.; Mesfin, K. G.; Oelkers, E. H.; Gislason, S. R., Rapid CO2 mineralisation into calcite at the CarbFix storage site quantified using calcium isotopes. Nat. Comm. 2019, 10 (1), 1983.

16.Trendafilova. 44.01 Signs Concession Agreement For Its First Demonstration CO2 Storage Project 2023. https://carbonherald.com/4401-signs-concession-agreement-for-its-first-demonstration-co2-storage-project/ (accessed July 26, 2024).

17.Rassenfoss, S., Mountains in Oman Can Store Huge Amounts of CO2 if a Way Can Be Found Into the Tight Rock. Journal of Petroleum Technology 2023, 75 (05), 28-33.

18.Oelkers, E. H.; Addassi, M.; Omar, A.; Afifi, A.; Hoteit, H.; Finkbeiner, T.; Menegoni, N.; Delaunay, A.; Fedorik, J.; Ahmed, Z. In The successful carbon storage through subsurface mineral carbonation in the volcanic rocks near Jazan, Southwest Saudi Arabia, 2024 Goldschmidt Conference, GOLDSCHMIDT: 2024.

19.Jacobs, J. E.; Stanfield, C. H.; Miller, Q. R. S.; Villante, M. A.; Marcial, J.; Nienhuis, E. T.; Silverstein, J. A.; Polites, E. G.; Bartels, M. F.; Gooch, B. T.; Liu, J.; Thakurta, J.; Lahiri, N.; Schaef, H. T., Technoeconomic Potential for Carbon Mineralization with Enhanced Recovery of Critical Minerals in the Pacific Northwest. ACS Sustainable Resource Management 2025.

20.Murchland, M. A. M., Q.R.S.; Nagurney, A.B.; Stanfield, C.H.; Lahiri, N.; Silverstein, J.A.; Teng, Y.; Nienhuis, E.T.; Engelhard, M.H.; Mulcahy, C.; Schaef, H.T. , CO2-Based Leaching of Sulfidic Peridotite Drives Critical Mineral Mobilization and Carbonate Precipitation. EarthArXiv 2025, Preprint

21.Ovshinsky, S. R.; Fetcenko, M. A.; Ross, J., A nickel metal hydride battery for electric vehicles. Science 1993, 260 (5105), 176-181.

22.Battery Nickel Demand Set to Triple by 2030 2024. https://source.benchmarkminerals.com/article/battery-nickel-demand-set-to-triple-by-2030.

23.Stanfield, C. H.; Miller, Q. R.; Battu, A. K.; Lahiri, N.; Nagurney, A. B.; Cao, R.; Nienhuis, E. T.; DePaolo, D. J.; Latta, D. E.; Schaef, H. T., Carbon Mineralization and Critical Mineral Resource Evaluation Pathways for Mafic–Ultramafic Assets. ACS Earth and Space Chemistry 2024.

24.Wang, F.; Dreisinger, D.; Barr, G. In Accelerated CO2 Mineralization and Simultaneous Critical Metal Recovery from Ultramafic Tailings, Conference of Metallurgists, Springer: 2023; pp 45-53.

25.Hamilton, J. L.; Wilson, S.; Morgan, B.; Harrison, A. L.; Turvey, C. C.; Paterson, D. J.; Dipple, G. M.; Southam, G., Accelerating mineral carbonation in ultramafic mine tailings via direct CO2 reaction and heap leaching with potential for base metal enrichment and recovery. Economic Geology 2020, 115 (2), 303-323.

26.Wang, F.; Dreisinger, D., Acceleration of Iron-Rich Olivine CO2 Mineral Carbonation and Utilization for Simultaneous Critical Nickel and Cobalt Recovery. Minerals 2024, 14 (8), 766.

27.Miller, Q. R. S.; Nagurney, A. B.; Blondes, M. S.; Thakurta, J.; Liu, J.; Gadikota, G.; Lahiri, N.; Schaef, H. T., Carbon-Negative Nickel Mining to Meet Global Mineral Resource Demands EarthArXiv 2025 Preprint

28.NS Energy. Tamarack Nickel Project 2022. https://www.nsenergybusiness.com/projects/tamarack-nickel-project/ (accessed July 25, 2024).

29.Raza, A.; Glatz, G.; Gholami, R.; Mahmoud, M.; Alafnan, S., Carbon mineralization and geological storage of CO2 in basalt: Mechanisms and technical challenges. Earth-Sci. Rev. 2022, 229.

30.Seifritz, W., CO2 disposal by means of silicates. Nature 1990, 345 (6275), 486-486.

31.Santos, R. M.; Van Audenaerde, A.; Chiang, Y. W.; Iacobescu, R. I.; Knops, P.; Van Gerven, T., Nickel Extraction from Olivine: Effect of Carbonation Pre-Treatment. Metals 2015, 5 (3), 1620-1644.

32.Li, X.; Nienhuis, E. T.; Nagurney, A. B.; Miller, Q. R. S.; Zhang, X.; Schaef, H. T., Resolving Nanoscale Processes during Carbon Mineralization Using Identical Location Transmission Electron Microscopy. Environ. Sci. & Technol. Lett. 2024, 11 (2), 79-88.

33.Taranovic, V.; Ripley, E. M.; Li, C.; Rossell, D., Petrogenesis of the Ni–Cu–PGE sulfide-bearing Tamarack Intrusive Complex, Midcontinent Rift System, Minnesota. Lithos 2015, 212-215, 16-31.

34.Taranovic, V.; Ripley, E. M.; Li, C.; Rossell, D., Chalcophile element (Ni, Cu, PGE, and Au) variations in the Tamarack magmatic sulfide deposit in the Midcontinent Rift System: implications for dynamic ore-forming processes. Mineralium Deposita 2016, 51 (7), 937-951.

35.Goldner, B. D., Igneous petrology of the Ni-Cu-PGE mineralized Tamarack intrusion, Aitkin and Carlton counties, Minnesota. 2011.

36.Jacobs, J. E.; Stanfield, C. H.; Miller, Q. R.; Villante, M. A.; Marcial, J.; Nienhuis, E. T.; Silverstein, J. A.; Polites, E. G.; Bartels, M. F.; Gooch, B. T., Technoeconomic Potential for Carbon Mineralization with Enhanced Recovery of Critical Minerals in the Pacific Northwest. ACS Sustainable Resource Management 2025.

37.Bartels, M. F.; Miller, Q. R.; Cao, R.; Lahiri, N.; Holliman Jr, J. E.; Stanfield, C. H.; Schaef, H. T., Parts-Per-Million Carbonate Mineral Quantification with Thermogravimetric Analysis–Mass Spectrometry. Analytical Chemistry 2024, 96 (11), 4385-4393.

38.Morfin, A. M.; Stanfield, C. H.; Murchland, M. A.; Bartels, M. F.; Nagurney, A. B.; Miller, Q. R. S.; Schaef, H. T., Structure–Composition Relationships for Mg–Ni and Mg–Fe Olivine. ACS Earth and Space Chemistry 2024.

39.Miller, Q. R. S.; Kaszuba, J. P.; Kerisit, S. N.; Schaef, H. T.; Bowden, M. E.; McGrail, B. P.; Rosso, K. M., Emerging investigator series: ion diffusivities in nanoconfined interfacial water films contribute to mineral carbonation thresholds. Environmental Science: Nano 2020, 7 (4), 1068-1081.

40.Miller, Q. R. S.; Schaef, H. T.; Kaszuba, J. P.; Qiu, L.; Bowden, M. E.; McGrail, B. P., Tunable Manipulation of Mineral Carbonation Kinetics in Nanoscale Water Films via Citrate Additives. Environmental Science & Technology 2018, 52 (12), 7138-7148.

41.Schaef, H. T.; Windisch, C. F., Jr.; McGrail, B. P.; Martin, P. F.; Rosso, K. M., Brucite [Mg(OH)2] carbonation in wet supercritical CO2: An in situ high pressure X-ray diffraction study. Geochim. Cosmochim. Acta 2011, 75 (23), 7458-7471.

42.Földvári, M., Handbook of thermogravimetric system of minerals and its use in geological practice. Geological Institute of Hungary Budapest: 2011; Vol. 213.

43.Demir, F.; Donmez, B.; Okur, H.; Sevim, F., Calcination kinetic of magnesite from thermogravimetric data. Chemical Engineering Research & Design 2003, 81 (A6), 618-622.

44.Miller, Q. R. S.; Thompson, C. J.; Loring, J. S.; Windisch, C. F.; Bowden, M. E.; Hoyt, D. W.; Hu, J. Z.; Arey, B. W.; Rosso, K. M.; Schaef, H. T., Insights into silicate carbonation processes in water-bearing supercritical CO2 fluids. International Journal of Greenhouse Gas Control 2013, 15, 104-118.

45.Mergelsberg, S. T.; De Yoreo, J. J.; Miller, Q. R. S.; Marc Michel, F.; Ulrich, R. N.; Dove, P. M., Metastable solubility and local structure of amorphous calcium carbonate (ACC). Geochimica et Cosmochimica Acta 2020, 289, 196-206.

46.Morse, J. W.; Arvidson, R. S., The dissolution kinetics of major sedimentary carbonate minerals. Earth-Science Reviews 2002, 58 (1-2), 51-84.

47.Qomi, M. J. A.; Miller, Q. R. S.; Zare, S.; Schaef, H. T.; Kaszuba, J. P.; Rosso, K. M., Molecular-Scale Mechanisms of CO2 Mineralization in Nanoscale Interfacial Water Films. Nature Reviews Chemistry 2022, 6, 598–613.

48.Palandri, J. L.; Kharaka, Y. K. A compilation of rate parameters of water-mineral interaction kinetics for application to geochemical modeling; Open File Report 2004-1068; United States Geological Survey: Menlo Park, California, 2004; p 64.

49.Johnson, N. C.; Thomas, B.; Maher, K.; Rosenbauer, R. J.; Bird, D.; Brown, G. E., Jr., Olivine dissolution and carbonation under conditions relevant for in situ carbon storage. Chem. Geol. 2014, 373, 93-105.

50.Zhang, S.; DePaolo, D. J., Rates of CO2 Mineralization in Geological Carbon Storage. Acc. Chem. Res. 2017, 50 (9), 2075-2084.

51.Thomas, B. J., Roger; Peters, Oliver; Pint, Christine November 2022 National Instrument 43-101 Technical Report of the Tamarack North Project – Tamarack, Minnesota; Talon Metals Copr. : 2022.

52. Correia, L. F., Tim; Gagnon, Daniel; Gravel, Andre-Francois; Liskovych, Volodymyr; Martin, Andrea; Peters, Oliver; Ritchie, David; Thomas, Brian Preliminary Economic Assessment (PEA) #3 of the Tamarack North Project – Tamarack, Minnesota; Talon Metals Corp.: 2021.

53.Sullivan, M.; Rodosta, T.; Mahajan, K.; Damiani, D., An overview of the Department of Energy's CarbonSAFE Initiative: Moving CCUS toward commercialization. AIChE Journal 2020, 66 (4), e16855.

54.Mineral commodity summaries 2025; 2025; Reston, VA, 2025; p 212.

Supporting Information

Nanoscale Interfacial Dissolution-Precipitation Reactions Drive Incipient Carbon Mineralization at the Tamarack Intrusive Complex Peridotite

Madeline F. Bartels [a†*], Quin R.S. Miller [a*], Xiaoxu Li [b], C. Heath Stanfield [a], Ruoshi Cao [a], Jose Marcial [a], Emily T. Nienhuis [b] Mathieu Fillion [c], Robert Rush [d], Martin Sauvé [e], H. Todd Schaef [a]

[a] Energy and Environment Directorate, Pacific Northwest National Laboratory, Richland, Washington, USA

[b] Physical and Computational Sciences Directorate, Pacific Northwest National Laboratory, Richland, WA, USA

[c] Rio Tinto, Montréal, Québec, Canada

[d] Rio Tinto, Salt Lake City, Utah, 84104, USA

[e] Rio Tinto, Ulaanbaatar Hot, Mongolia

[†] Current affiliation is Department of Earth, Energy, & Environment, University of Calgary, Calgary, AB, Canada

[*]Corresponding authors' contact information:
madeline.bartels@ucalgary.ca
quin.miller@pnnl.gov

13 Pages
5 Figures
5 Tables

METHODS

Helium Pycnometry. Helium pycnometry was performed with a Micromeritics AccuPyc II 1340 gas pycnometer on Tamarack grains with an aliquot mass of 2.2174 g in a 3.5 cm3 sample chamber that had been calibrated using the manufacturer's standard. Samples were measured 10 times and averaged to obtain the final density.

Electron Probe Microanalysis (EPMA). EPMA was used for spot analysis (using a 10 µm defocused beam) and elemental mapping (using a focused beam) with 15kV accelerating voltage and 15nA probe current. Prior to measurement, grains were mounted in epoxy and polished using 400, 600, 800, and 1200 grit SiC grinding paper and 1 µm diamond polishing compound. Natural and synthetic standards were utilized for peak position calibration and X-ray intensity calibration using ProbeforEPMA software. For quantification, a time-dependent intensity (TDI) correction was applied to Na.

Thermogravimetric Analysis – Mass Spectrometry (TGA-MS). Unreacted and reacted Tamarack Bowl-1 and Hybrid powders were analyzed with TGA-MS to detect and quantify hydrated/hydroxylated and carbonate minerals. Measurements were conducted on a 2022 Netzsch TG 209 F1 Libra Thermo Micro Balance coupled to a Netzsch QMS 403 Aëolos Quadro mass spectrometer with a 300 °C heated capillary inlet system. Prior to measurement, the crucible was run under a TGA-MS heating regimen of 10 °C min-1 from ~30 °C to 1,000 °C to create a correction file for buoyancy factors associated with unique crucible weights. ~20 mg of powdered sample was placed in an 85 µl corundum crucible and run under the heating regimen described above, and ion currents for CO2 (m/z=44) and H2O (m/z=18) were monitored simultaneously. The carbonation reaction extent was calculated by obtaining weight percent magnesite in two ways: 1) comparing the experimental TGA mass loss with the theoretical mass loss for a pure carbonate sample and 2) a modified method using calcium oxalate monohydrate calibration curves. The uncertainty in this quantification method is ≤ 0.5 wt%1.

Powder X-ray Diffraction (XRD). X-ray diffraction analysis was conducted on the pre- and post-reaction Hybrid sample rock mixture with our Bruker D8 Discover TXS-HE XRD system. XRD scans were collected using a Bruker D8 Discover TXS-HE A25, equipped with a rotating Cu anode (Kα λ = 1.54060 Å), 0.3 x 3 mm cassette tungsten filament, Atlas goniometer, and a UMC 1516 motorized xyzϕχ stage. Powdered Hybrid Tamarack samples prepared with an agate mortar and pestle were mounted in a low-background silicon powder mount on the stage and positioned using a laser-video alignment system. The power settings of the generator were set to 45 kV and 120 mA, and the source-sample distance was 425 mm. The scans were collected with the instrument in Bragg-Brentano geometry with a Ni filter, a 0.6 mm divergence slit, and a 2.5° axial Soller. A panoramic 2.5° Soller attachment was placed on the Dectris EIGER2 R 500K detector, and the detector was placed in 1D mode with an active area of 65 x 20 mm. Scans were collected from 10-80 °2θ in coupled 2θ/θ mode with 3501 steps at an increment of 0.02 and continuous stage rotation (ϕ) at 360 °/min. Scans were then imported into Bruker EVA6.0 software for phase identification using the International Center for Diffraction Database (ICDD) powder diffraction file (PDF) 5+ 2024 database. Bruker AXS TOPAS 6 was used for quantitative Rietveld Refinement of the sample using phases identified in EVA6. The background was calculated using a 10th order Chebychev polynomial and the crystallite size of the individual phases was modeled with a Lorentzian contribution to the peak width. Mineral abundances are generally accurate to within ~±5 wt% 2, 3.

Batch Reaction Carbonation Experiments. To simulate a range of potential reservoir conditions, Bowl-1 and Hybrid samples were reacted at 90 bar and 21, 50, or 90 °C. Although the exact TIC reservoir conditions vary from these temperatures, higher temperatures were chosen to accelerate kinetics, and geochemical calculations suggest that the water-rock interactions are the same as those predicted at lower temperatures 4. This approach has also been used in similar experimental studies on CO_2-water-rock interactions at supercritical conditions 2, 5-10. A pressure of 90 bar was chosen to maintain supercritical CO_2 conditions and simulate a reservoir condition corresponding to a depth of ~0.8-1 km. This pressure is also consistent with previous studies investigating reactivity of mafic-ultramafic minerals in scCO_2 2, 11, 12. For the aqueous-dissolved experiments, 2.5 g of sample was submerged in 15 mL of water in a 25 mL Parr vessel reactor. For the wet scCO_2 experiments, 10 mL of water was put in the bottom of the reactor and a 2 g sample was set on a Teflon tripod out of direct contact with the water. Several samples reacted with wet scCO_2 were set in individual 15 mL polypropylene centrifuge tubes which were collectively placed into a 300 mL Parr vessel reactor. All Parr reactors contain a valve, pressure gauge, and burst disc. 90 mL of water was added to the bottom of the vessel, out of contact with the samples. Each vessel used in 50 and 90 °C experiments was then sealed and kept at temperature in a laboratory oven (Quincy Model 10 or Lindberg/Blue Model MO1450A-1). Once the vessel had equilibrated to 50 or 90 °C, it was then pressurized to 90 bar by CO_2 gas (>99.999%) and sealed again. Reacted samples were removed from vessels and dried in an ambient temperature vacuum oven.

Identical Location Transmission Electron Microscopy (IL-TEM). A suspension (~1 g/L) of the Tamarack Bowl-1 sample was prepared with Milli-Q water and sonicated for five minutes. 100 µL of sample was dropped onto 200 mesh gold TEM grids (Lacey Carbon, 300 mesh; Ted Pella, Inc) and air dried. An FEI Titan 80-300 Environmental TEM microscope with an objective lens corrector recorded initial images and locations of the sample on the grids as a Gatan 626 single tilt cryo-holder kept the sample temperature below -170 °C. The dose rate during imaging was maintained lower than 20 $e^-/Å^2$ to ensure that the sample material was stable13. The nanoparticle-loaded TEM grids were then placed on a perforated Teflon tripod inside a 25 mL high-pressure Parr vessel, following the methods of Li, Nienhuis, Nagurney, Miller, Zhang and Schaef 13. 100 µL Milli-Q water, an amount sufficient to fully saturate the scCO_2 at 50 °C and 90 bar 2, was dropped in the bottom of reactor out of direct contact with the mineral sample or TEM grid. The Parr vessels were sealed, preheated to 50 °C in an oven, and pressurized to 90 bar by CO_2 gas (>99.999%), exposing the minerals to a scCO_2 fluid with 0.354 mol% H_2O content 14 and a density of ~285 kg/m^3 15. After the sample reacted with scCO_2 for 21 days, the Parr vessels were depressurized and TEM grids were immediately placed in a vacuum desiccator for one hour to desorb adsorbed CO_2 and prevent quench reactions. Identical sample locations were imaged by TEM with a Gatan 626 liquid nitrogen cryo-holder, and Energy-Dispersive Spectroscopy (EDS) with a QUANTAX EDS detector (Bruker Inc.) to obtain nanoscale-resolved pre- and post-reaction crystallographic images.

SUPPORTING INFORMATION FIGURES

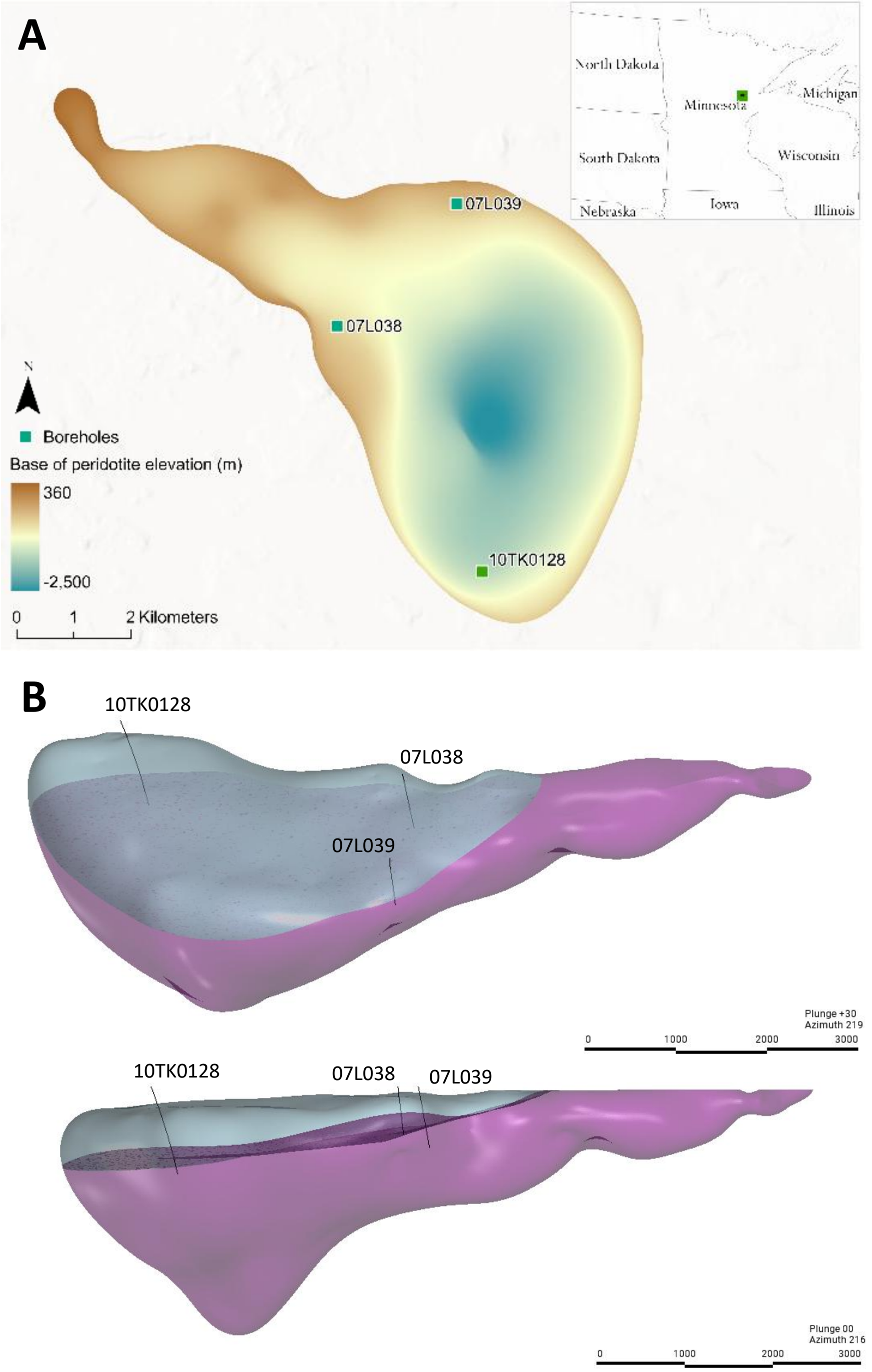

Figure S1. The bowl-shaped peridotite intrusion in the Tamarack Intrusive Complex, Minnesota, USA. The Bowl-1 sample was retrieved from a 2010 legacy borehole, 10TK0128. Two cores from borehole 07L038 and one core from borehole 07L039 were combined to create the Hybrid sample.

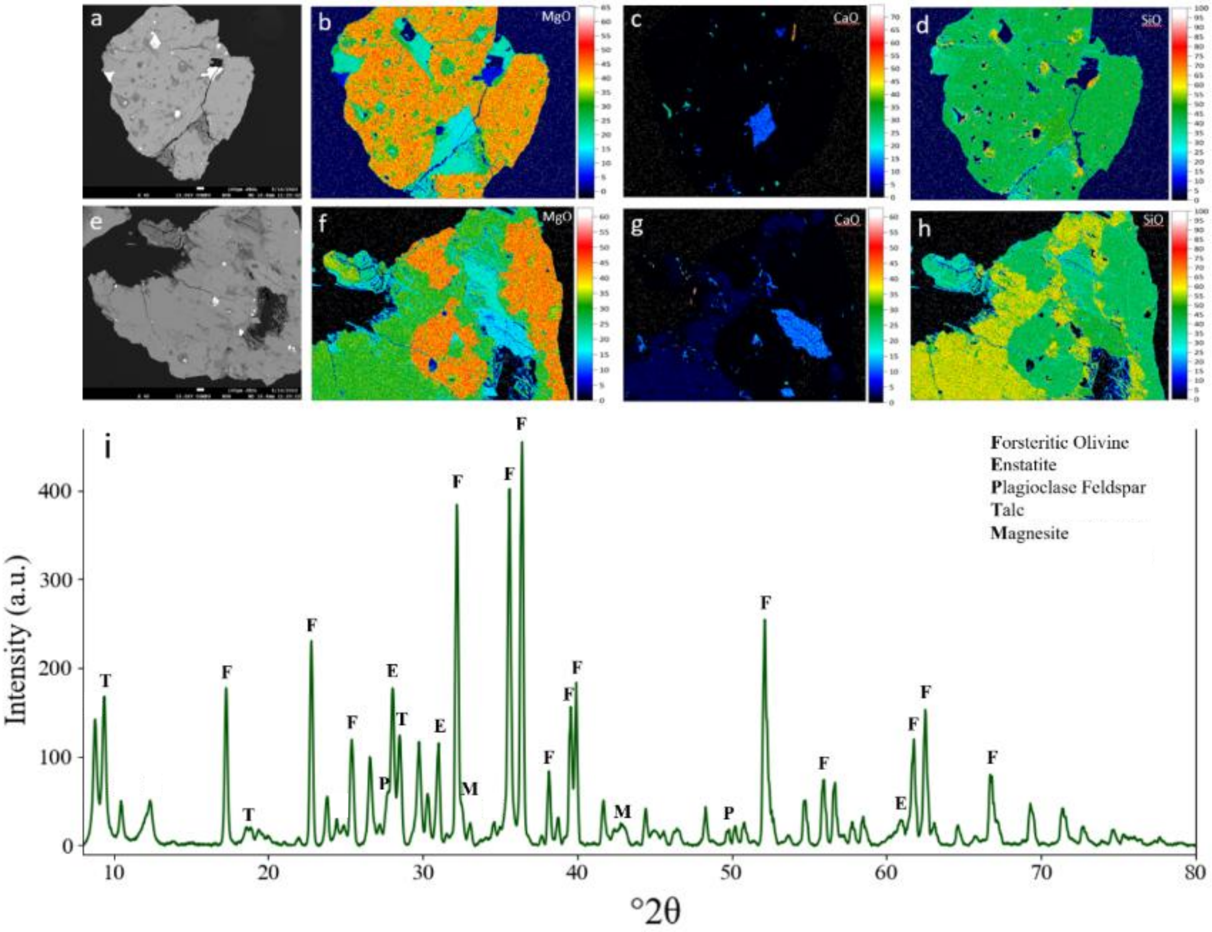

Figure S2. Geochemical and mineralogical characterization of the Tamarack Bowl intrusion olivine (BIO) samples was accomplished with a suite of techniques including EPMA (a-h) and XRD (i). (a, e) Bowl-1 grains selected for EPMA geochemical mapping with (b, f) MgO abundance, (c, g) CaO abundance, and (d, h) SiO_2 abundance reported in weight percent. (i) XRD mineralogical phase analysis reveal sample composition to be a peridotite with major forsteritic olivine content and lesser pyroxene and plagioclase feldspar content.

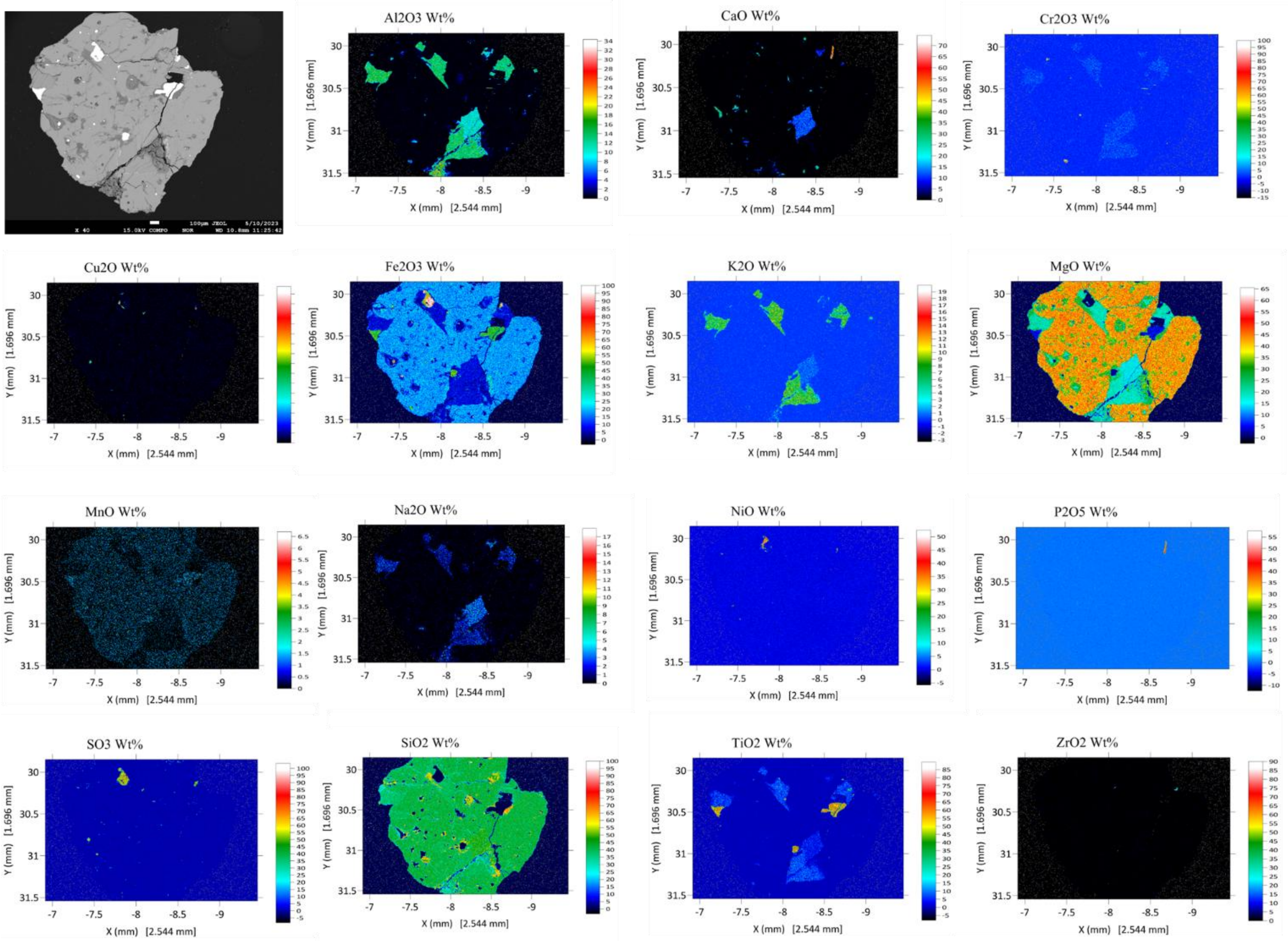

Figure S3. Electron Probe Microanalysis (EPMA) of the TIC Bowl-1 sample grain #1.

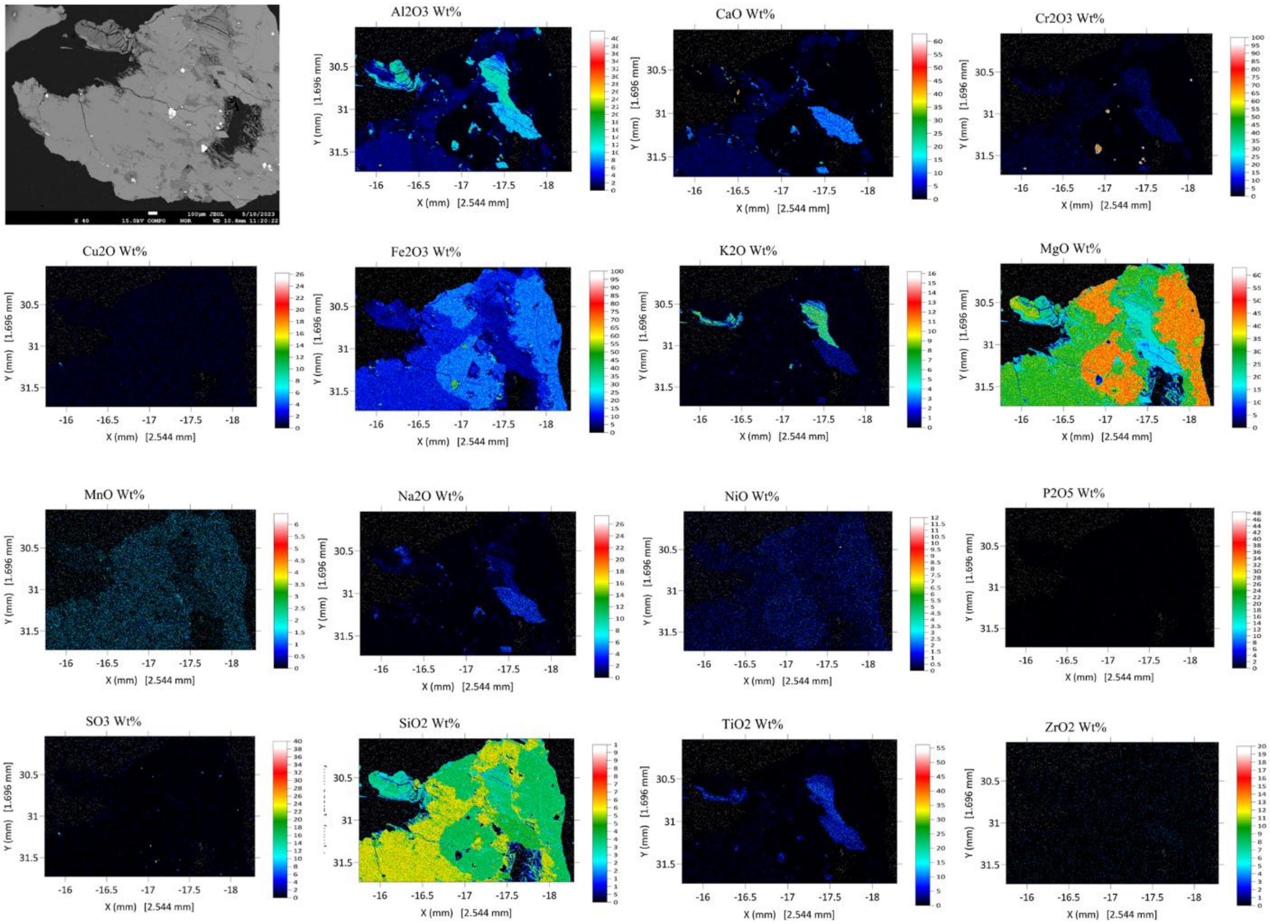

Figure S4. Electron Probe Microanalysis (EPMA) of the TIC Bowl-1 sample grain #2.

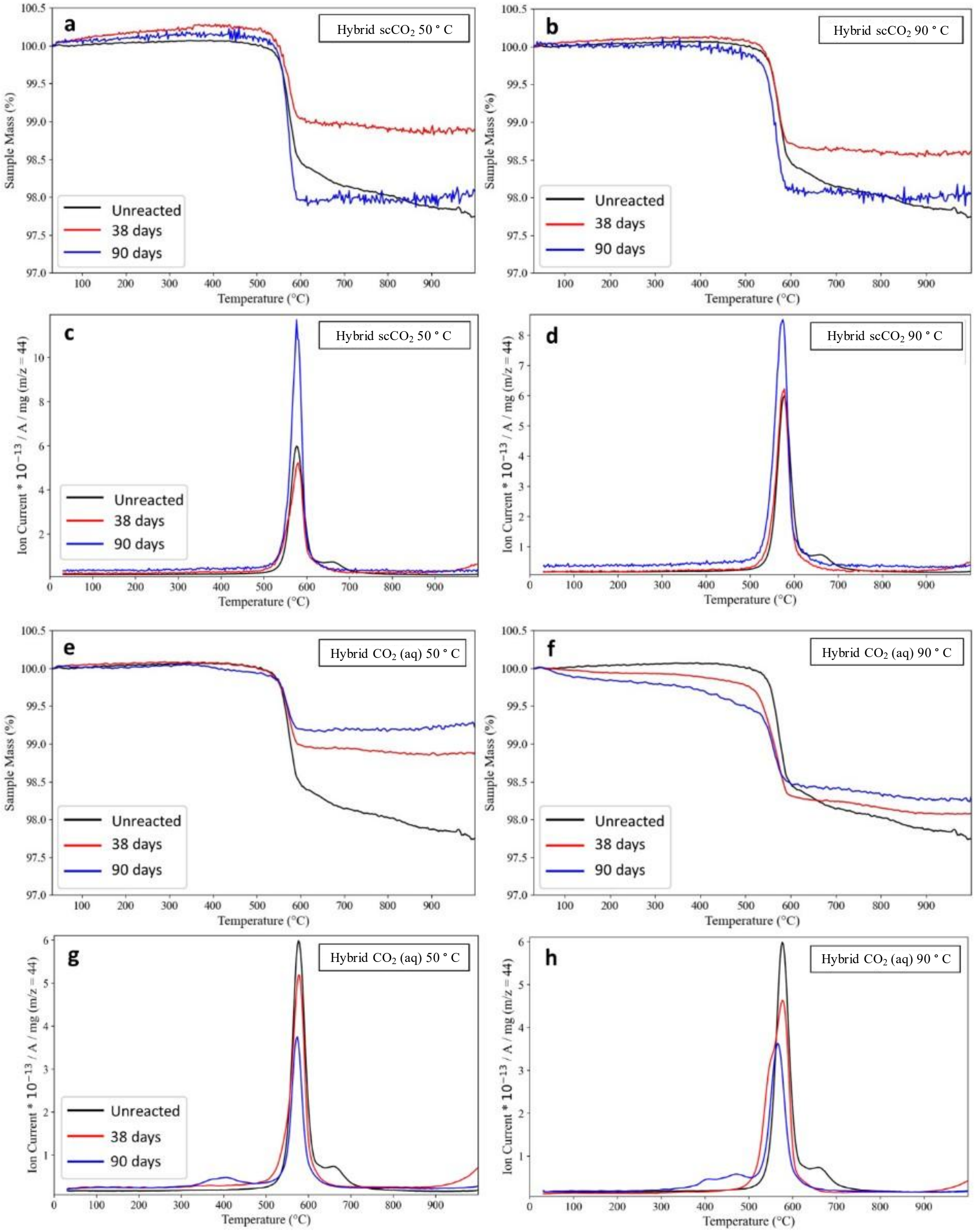

Figure S5. (a, b, e, f) Thermogravimetric analysis – mass spectrometry (TGA-MS) sample weight loss curves for Parr vessel carbonation experiments of a Tamarack Hybrid sample reacted with $scCO_2$ and CO_2 (aq) at 90 bar, 50 °C and 90 °C. Sample mass loss in the 550-650 °C temperature range is due to magnesite decomposition to MgO and CO_2. (c, d, g, h) Evolved CO_2 ion current curves for the same experiments. The coupled mass spectrometer measures CO_2 (m/z 44) ion current and the amount of CO_2 released is quantified by taking the area under the curve.

SUPPORTING INFORMATION TABLES

Table S1. Quantitative mineralogy of the unreacted Tamarack Bowl-1 and Hybrid samples obtained from X-ray diffraction.

Sample	**Bowl-1**	**Hybrid**
Mineral (ICDD PDF#)	(wt%)	(wt%)
Anorthite (00-041-1486)	9	8
Clinochlore (01-089-6455)	--	5
Enstatite (01-076-2426)	10	11
Fe-bearing Forsterite (01-075-1556)	72	65
Hornblende (01-085-2159)	--	2
Magnesite (01-083-1761)	2	4
Talc (04-010-7170)	7	5

Table S2: Helium pycnometry-derived Tamarack sample densities.

	Density (g/cm^3)
Bowl-1	3.2665
Hybrid	3.354

Table S3. Oxide abundances derived from ten Electron Probe Microanalysis (EPMA) point scans of the TIC Bowl-1 sample.

Point	**1**	**2**	**3**	**4**	**5**	**6**	**7**	**8**	**9**	**10**
Na_2O	0.037	-0.004	0.012	-0.007	0.319	0.029	2.925	0.008	0.874	1.71
CaO	1.996	0.082	0.059	0.072	0.078	2.07	11.452	-0.002	0.166	0.016
K_2O	0.024	0.013	0.036	0.018	0.037	0.022	0.651	0.04	0.011	7.009
MgO	29.586	44.003	0.007	43.408	28.709	29.872	15.761	4.348	30.063	19.293
Al_2O_3	1.793	0.014	0.003	0.017	0.771	1.671	9.874	-0.027	2.075	13.739
SiO_2	58.179	41.476	0.022	41.616	58.877	57.707	45.888	0.032	56.995	40.065
Fe_2O_3	10.632	17.741	47.308	17.541	5.346	10.694	7.461	45.194	3.987	6.564
TiO_2	0.289	0.042	0.014	0.033	0.043	0.302	3.735	53.769	0.074	6.091
MnO	0.195	0.228	0.027	0.235	0.018	0.212	0.06	0.62	0.007	-0.015
ZrO_2	-0.02	-0.013	0.016	0.035	0.037	-0.026	0.154	0.03	0.03	-0.02
P_2O_5	0.011	0	0.016	-0.01	0.013	-0.004	0.04	0.001	0.011	-0.005
NiO	0.074	0.215	0.725	0.23	0.037	0.041	0.069	0.037	0.059	0.089
Cu_2O	0.044	0.016	38.839	0.042	0.002	-0.052	-0.008	-0.027	0.014	0.021
SO_3	-0.007	-0.021	56.913	-0.003	0.047	0.002	-0.04	-0.143	0.003	0
Cr_2O_3	1.293	0.09	0.075	0.105	0.62	1.171	1.762	0.713	0.156	2.659
Total	104.125	103.88	144.071	103.331	94.954	103.711	99.783	104.592	94.525	97.215

Table S4. Experimental conditions and post-reaction magnesite abundance for Tamarack Bowl-1 and Hybrid (0.425-2 mm size fractioned) sample experiments conducted at 21-90 °C under aqueous-dissolved CO_2 (CO_2 (aq)) and supercritical CO_2 (scCO_2).

Experiment [a]	**Reaction fluid**	**Temperature (°C)**	**Reaction time (days)**	**Sample mass (g)**	**Water volume (mL)**	**TGA-MS magnesite abundance** [b] **(wt%)**
Bowl-1 scCO_2	scCO_2	50	160	2	90	2.8
		90	56			3.9
		21	270			3.4
Hybrid scCO_2		50	38			1.9
			90			3.2
Hybrid CO_2 (aq)	CO_2 (aq)		38	2.5	15	1.8
			90			1.4
Hybrid scCO_2	scCO_2	90	38	2	90	2.0
			90			2.8
Hybrid CO_2 (aq)	CO_2 (aq)		38	2.5	15	2.2
			90			1.7

[a] All experiments were conducted at 90 bar CO_2 pressure. H_2O solubility in 90 bar scCO_2 (mol %) is 1.359 and 0.354 for 90 °C and 50 °C, respectively, based on the solubility model of Spycher and Pruess.[55]

[b] Magnesite abundance values were calculated from the TGA-MS's mass spectrometer reading of evolved CO_2 ion current.

Table S5. CO_2 storage potential and Ni mobilization potential of the Tamarack BIO. We assume that injected fluids access 5% of the BIO's reactive surface area and that all Mg^{2+} and Fe^{2+} ions are released upon olivine dissolution, combining with fluid phase CO_2 to form carbonate minerals. We also assume all olivine-hosted Ni is mobilized into the fluid phase during 5% BIO dissolution. BIO rock density is 3.3 g/cm^3 (obtained from helium pycnometry), weight percent olivine in the BIO reservoir is 65% (obtained from XRD), and concentration of Ni in olivine is 1700 ppm (obtained from EPMA). MMT = million metric tonnes.

Reservoir volume (km^3)	**Porosity** (%)	**CO_2 storage potential** (MMT)	**Ni mobilization potential** (MMT)	**CO2**
18	5	1066	3.12	
18	10	1010	2.95	
18	15	954	2.79	
12	5	711	2.08	
12	10	673	1.97	

Supplemental References

(1) Bartels, M. F.; Miller, Q. R. S.; Cao, R.; Lahiri, N.; Holliman, J. E., Jr.; Stanfield, C. H.; Schaef, H. T. Parts-Per-Million Carbonate Mineral Quantification with Thermogravimetric Analysis–Mass Spectrometry. Anal. Chem. 2024, 96 (11), 4385-4393. DOI: 10.1021/acs.analchem.3c03936.

(2) Miller, Q. R. S.; Kaszuba, J. P.; Schaef, H. T.; Bowden, M. E.; McGrail, B. P. Impacts of organic ligands on forsterite reactivity in supercritical CO2 fluids. Environ. Sci. Technol. 2015, 49 (7), 4724-4734. DOI: 10.1021/es506065d.

(3) Miller, Q. R. S.; Kaszuba, J. P.; Kerisit, S. N.; Schaef, H. T.; Bowden, M. E.; McGrail, B. P.; Rosso, K. M. Emerging investigator series: ion diffusivities in nanoconfined interfacial water films contribute to mineral carbonation thresholds. Environ. Sci. Nano 2020, 10.1039/C9EN01382B. DOI: 10.1039/C9EN01382B.

(4) Marcon, V.; Kaszuba, J. P. Carbon dioxide-brine-rock interactions in a carbonate reservoir capped by shale: Experimental insights regarding the evolution of trace metals. Geochimica Et Cosmochimica Acta 2015, 168, 22-42. DOI: 10.1016/j.gca.2015.06.037.

(5) Gunter, W. D.; Wiwchar, B.; Perkins, E. H. Aquifer disposal of CO2-rich greenhouse gases: Extension of the time scale of experiment for CO2-sequestering reactions by geochemical modelling. Mineralogy and Petrology 1997, 59 (1-2), 121-140. DOI: 10.1007/bf01163065.

(6) Credoz, A.; Bildstein, O.; Jullien, M.; Raynal, J.; Petronin, J. C.; Lillo, M.; Pozo, C.; Geniaut, G. Experimental and modeling study of geochemical reactivity between clayey caprocks and CO2 in geological storage conditions. In Greenhouse Gas Control Technologies 9, Gale, J., Herzog, H., Braitsch, J. Eds.; Energy Procedia, Vol. 1; Elsevier Science Bv, 2009; pp 3445-3452.

(7) Alemu, B. L.; Aagaard, P.; Munz, I. A.; Skurtveit, E. Caprock interaction with CO2: A laboratory study of reactivity of shale with supercritical CO2 and brine. Appl. Geochem. 2011, 26 (12), 1975-1989. DOI: 10.1016/j.apgeochem.2011.06.028.

(8) Schaef, H. T.; Windisch, C. F., Jr.; McGrail, B. P.; Martin, P. F.; Rosso, K. M. Brucite [Mg(OH)2] carbonation in wet supercritical CO2: An in situ high pressure X-ray diffraction study. Geochim. Cosmochim. Acta 2011, 75 (23), 7458-7471. DOI: 10.1016/j.gca.2011.09.029.

(9) Loring, J. S.; Thompson, C. J.; Wang, Z.; Joly, A. G.; Sklarew, D. S.; Schaef, H. T.; Ilton, E. S.; Rosso, K. M.; Felmy, A. R. In Situ Infrared Spectroscopic Study of Forsterite Carbonation in Wet Supercritical CO2. Environmental Science & Technology 2011, 45 (14), 6204-6210. DOI: 10.1021/es201284e.

(10) Loring, J. S.; Schaef, H. T.; Turcu, R. V. F.; Thompson, C. J.; Miller, Q. R. S.; Martin, P. F.; Hu, J. Z.; Hoyt, D. W.; Qafoku, O.; Ilton, E. S.; et al. In Situ Molecular Spectroscopic Evidence for CO2 Intercalation into Montmorillonite in Supercritical Carbon Dioxide. Langmuir 2012, 28 (18), 7125-7128. DOI: 10.1021/la301136w.

(11) Miller, Q. R. S.; Kaszuba, J. P.; Schaef, H. T.; Thompson, C. J.; Qiu, L.; Bowden, M. E.; Glezakou, V. A.; McGrail, B. P. Experimental study of organic ligand transport in supercritical CO2 fluids and impacts to silicate reactivity. Energy Procedia 2014, 63 (0), 3225-3233. DOI: http://dx.doi.org/10.1016/j.egypro.2014.11.349.

(12) Loring, J. S.; Schaef, H. T.; Turcu, R. V. F.; Thompson, C. J.; Miller, Q. R. S.; Martin, P. F.; Hu, J.; Hoyt, D. W.; Qafoku, O.; Ilton, E. S.; et al. In Situ Molecular Spectroscopic Evidence for CO2 Intercalation into Montmorillonite in Supercritical Carbon Dioxide. Langmuir 2012, 28 (18), 7125-7128. DOI: 10.1021/la301136w.

(13) Li, X.; Nienhuis, E. T.; Nagurney, A. B.; Miller, Q. R. S.; Zhang, X.; Schaef, H. T. Resolving Nanoscale Processes during Carbon Mineralization Using Identical Location Transmission Electron Microscopy. Environ. Sci. & Technol. Lett. 2023. DOI: 10.1021/acs.estlett.3c00699.

(14) Spycher, N.; Pruess, K. A Phase-Partitioning Model for CO2-Brine Mixtures at Elevated Temperatures and Pressures: Application to CO2-Enhanced Geothermal Systems. Transport Porous Med. 2010, 82 (1), 173-196, Article. DOI: 10.1007/s11242-009-9425-y.

(15) Span, R.; Wagner, W. A new equation of state for carbon dioxide covering the fluid region from the triple-point temperature to 1100 K at pressures up to 800 MPa. Journal of Physical and Chemical Reference Data 1996, 25 (6), 1509-1596.